Postprint version of article published as:
Ausland, L., Revheim, M. E., Skretting, A., & Stokke, C. (2017). Respiratory motion during 90Yttrium PET contributes to underestimation of tumor dose and overestimation of normal liver tissue dose. Acta Radiologica, 0284185117710052.

Respiratory motion during ^{90}Yttrium PET contributes to underestimation of tumor dose and overestimation of normal liver tissue dose

Abstract

Background: Yttrium-90 dosimetry after radioembolization is reliant on accurate quantitative imaging of the microsphere deposition. Previous studies have focused on the correction of geometrical resolution effects.

Purpose: To uncover additional effects of respiratory motion.

Material and Methods: Mathematical models describing spherical tumors were formed, and two blurring effects, limited geometrical resolution and respiratory motion, were simulated. The virtual images were used as basis for dose volume histogram estimations by convolving the radioactivity representations with a dose point kernel.

Results: For respiratory motion only, the largest errors were found for the smallest tumors and/or tumors with heterogeneous distribution of yttrium-90 microspheres. The deviations in max dose and dose to 25% and 50% of the tumor volume were estimated 20-40%, 10-30% and 0-30%, respectively. Additional blurring from geometrical resolution increased the errors to 55-75%, 50-60% and 25-60%, respectively.

Conclusion: Respiratory motion contributes to underestimation of tumor dose and overestimation of normal tissue dose.

Keywords: Yttrium-90, PET, Radionuclide Therapy, SIRT, respiratory motion

Introduction

Liver metastases are often therapeutically challenging, however, techniques such as stereotactic radiotherapy, radiofrequency ablation and radioembolization have a promising role for patients with unresectable disease (1). Radioembolization, or selective internal radiation therapy (SIRT), is based on the nature of the tumor vasculature, allowing delivery of isotopes with short ranged radiation directly to the tumors. Yttrium-90 loaded microspheres are delivered to the tumor via the hepatic artery, from which liver malignancies receive most of their blood supply. Because the normal liver tissue is supplied mainly by the portal vein, this approach will potentially spare healthy tissue from radiation damage.

1 GBq ^{90}Y per kilogram of liver tissue with a uniform distribution of microspheres provides 50 Gy radiation dose to the whole organ (2). Even though the fraction to tumor tissue can be assumed higher than to normal tissue due to vasculature, the delivery of typically 2-3 GBq ^{90}Y calls for a close control and investigation of dose distribution. Sarfaraz and co-workers estimated mean absorbed doses to tumor and normal liver tissue of 163 Gy and 58 Gy, respectively, in a patient treated with glass microspheres for hepatocellular carcinoma (3). The study was based on ^{90}Y bremsstrahlung SPECT, and was the first report of direct quantitative imaging for SIRT dosimetry. Later, PET imaging was introduced, and a mean dose to tumors of 104 Gy was estimated for a patient with colorectal liver metastases treated with resin microspheres (4). An area of healthy liver tissue close to the tumor site was found exposed to 29 Gy. Mean tumor doses of 77-425 Gy were found for 11 patients in a later work (5), and Srinivas et al. reported mean tumor doses of 169 Gy (range: 0-570 Gy) and mean normal tissue doses of 67 Gy in 56 patients with hepatocellular carcinomas (6).

Accurate quantitative imaging of the deposition of microspheres is a requirement for reliable estimations of absorbed dose. The potential for reproducible activity quantitation across different PET systems has been demonstrated (7). ^{90}Y PET images suffers from poor count statistics because of the very low positron abundance of ^{90}Y (8). The PET-scanners inherent limited geometrical resolution also degrades the activity distribution image, by blurring. Correction for this blurring has been investigated by several groups (4, 9, 10). Respiratory movement is a

known challenge in ^{18}F-FDG PET imaging of the liver (11), but to the authors' knowledge, no previous work has been performed on the dosimetric impact of respiratory motion during ^{90}Y PET imaging after SIRT. By simulating dose volume histograms, the aim of this study was to illustrate the potential errors made in calculated dose to tumor and normal liver tissue by using ^{90}Y PET as basis for microsphere distribution.

Material and Methods

Tumor models

All simulations and calculations were performed with the interactive data language (IDL, ITT visual solutions, Boulder, CO, USA). In this work we assumed, for illustration purposes, zero image noise. Perfect spheres with radiuses of 6, 12, 15, 24 and 36 mm were assumed to represent tumors. Voxel sizes of 1x1x1 mm^3 and 3x3x3 mm^3 were chosen. Two microsphere distribution models founded the basis of the simulations, homogeneous and heterogeneous microsphere distribution.

Homogeneous microsphere distribution: The microspheres were assumed uniformly distributed in the spheres. As a homogeneous microsphere distribution throughout the volume seems especially unlikely for larger tumors, it was assumed irrelevant for the largest tumor models.

Heterogeneous microsphere distribution: Microscopy studies of whole livers or tissue samples have shown that both glass and resin microspheres concentrate in the outer rim of tumors (12, 13). According to biopsy studies, the resin microsphere density in normal tissue and in the tumor center is much less than in the periphery of the tumor (13). We will for illustration purposes assume an average heterogeneous distribution described by this work of Campbell et al. (Fig. 1C).

Blurring effects and image scenarios

For the distributions, two blurring effects resulting in three different imaging scenarios were simulated:

Ideal PET imaging: The image of the microsphere distribution before any modifications is called scenario 1 = ideal PET imaging (Fig. 1 A and B, left panel). This represents the true microsphere distribution and gives the real dose distribution.

Image blurring from respiratory motion: A sine function with an amplitude of 5 mm was assumed to represent respiratory motion (14), and image blurring caused by respiration was

simulated by convolution in the cranio-caudal direction. The resulting image is called scenario 2 = perfect resolution/respiratory movement (Fig. 1 A and B, mid panel).

Image blurring by point spread function (*PSF):* We simulated geometric resolution according to our PET system, a Siemens Biograph 64 scanner (Siemens Healthineers, Erlangen, Germany). The resolution power with voxels 2.67x2.67x2.025, ordered subset expectation-maximization reconstruction algorithm with 4 iteration and 8 subsets and a Gaussian filter of 5 mm full widths at half maximum, is 7.2 mm and 6.3 mm in the axial and longitudinal direction, respectively (15). A 3D Gaussian PSF describing the resolution power was made, and a 3D convolution with the image blurred by respiration resulted in a new scenario. This scenario describes the combined blurring effects, called scenario 3 = respiratory movement plus PSF blurring (Fig. 1 A and B, right panel).

Dosimetry

Yttrium-90 is a beta-emitter which decays with an average energy of 0,94 MeV, half-life of 64 h and an average and maximum tissue penetration of 2,5 mm and 1,1 cm, respectively (16). A beta dose point kernel (DPK) was obtained from tables of MIRD-pamphlet no 7 (17). The absorbed fraction of beta radiation was calculated by regression analysis with a fifth grade polynomial on a carthesian grid. The dose distributions for the scenarios were obtained by convolving the ^{90}Y activity simulations with the DPK, and then multiplying with the equilibrium dose, D_{eq}, given by Equation 1.

$$D_{eq} = \frac{\tilde{A}}{m} \cdot \overline{E} \qquad \text{(Eq.1)}$$

In Equation 1, m is the mass, $\tilde{A}$ the cumulated activity and $\bar{E}$ the average beta energy. Because the microspheres are permanent implants, $\tilde{A}$ is derived by the physical half-life. We assumed the following based on typical patient values at our hospital: a) a total liver lobe volume of 1000 ml (i.e. 1 kg) with density 1 g/cm^3, b) an activity of 1 Gq of ^{90}Y, c) a 90/10 % microsphere distribution between malignant and benign tissue respectively, d) a 20 % tumor burden and e) that the tumors retain microspheres proportionally to their size.

Tumor tissue dosimetry: Resulting dose volume histograms (DVHs) were plotted for all scenarios and radiuses. The dose distributions inside and around the spheres are reported, leaving out the bin with the smallest voxel values (from 0 Gy to x Gy depending on bin size x). In addition, max dose, D_{25} and D_{50} were found. All DVHs are reported using a voxel size of 3x3x3 mm^3, while as the tables quantify the results from the DVHs, the smaller voxel dimensions (1x1x1 mm^3) were chosen for tables.

Normal hepatic tissue dosimetry: To find the dose contribution from microspheres that lodge in the tumor periphery, the area corresponding to the inside of the tumor volume was removed, giving the dose distribution in normal tissue only. The resulting DVHs are reported, in addition to the max dose, and the D_{10} and D_{25} fractions. The volume in the 1000 ml liver lobe (minus the tumor volume) with a positive dose value is also reported. The average dose from the microspheres that distributes from the hepatic artery to the normal liver tissue was also estimated, using the assumptions described above.

Results

Tumor tissue

The blurring effects of image scenario 2 and 3 lead to a ^{90}Y uptake image larger than the actual tumor (Fig. 1), assigning dose values to surrounding voxels with little or no real absorbed dose. Image scenario 1 reflects the "real" dose distribution in this simulated situation. Fig. 2 b and d show DVHs for the homogeneous microsphere distribution. The dosimetric errors from blurring are not surprisingly found largest for the small spheres, and there are discrepancies between both maximum dose and minimum dose to 25 % or 50 % of the tumor volume (D_{25} and D_{50}) for the different scenarios (Table 1). For example, dose values deviations of approximately 20-30 % are observed when respiratory blurring is applied (scenarios 1 vs 2), and of 55-60 % for combined blurring effects (scenarios 1 vs 3), for 6 mm radius spheres. For spheres of 24 mm radius the size exceeds the borders of the blurring effects (using our parameters) and the maximum dose is identical, but still some differences exist between D_{50} values.

Although the same activity per volume is administrated to the tumors with heterogeneous microsphere distributions, the higher maximum doses are now due to an applied radial distribution with microspheres densely packed in the periphery (Table 2). In general, the same trend as for the homogeneous distributions can still be seen here; both blurring scenarios will cause a certain false spread of dose for the voxels. The sinusoidal respiratory motion will move the imaged high-density microsphere area (the periphery of the tumor), resulting in dose peaks of scenario 2 and 3 shifted towards lower values (Fig. 2 a, c and e). Here, the combined blurring effects cause the maximum dose value to never reach the actual maximum value. The overall deviations are worst for the smallest spheres of 6 mm radius. For the larger spheres, max dose and D_{25} deviations of approximately 0-25 % are observed between scenarios 1 and 2, and of 20-40 % between scenarios 1 and 3. For our parameters the D_{50} values tended to show the best numerical agreement, however, the D_{50} values could actually be overestimated due to the image misplacements of the periphery.

Normal hepatic tissue

Fig. 3 shows DVHs of the normal liver tissue in the ”treated” liver lobe, for a 24 mm tumor radius, obtained by removing the actual tumor area (as it would be presented by co-registered CT imaging). As expected in an ideal image situation (scenario 1), the dose to normal tissue from the microspheres lodged in the tumor falls rapidly to zero. In scenario 3, the blurring of both respiration motion and PSF causes the dose distribution to spread throughout the normal liver tissue. The “real” dose distributions demonstrate somewhat higher dose values for the homogeneous simulations. This is due to the low-density microsphere rim, at the outmost tumor periphery, described by the heterogeneous distribution. Interestingly, although the image scenario 2 histogram is closer to the image scenario 1 histogram, image scenario 2 demonstrates the highest max value to normal tissue (Tables 3 and 4). This is again the result of the mismatch between imaged and actual microsphere locations, combined with a missing/corrected PSF blurring. Adding PSF blurring spreads the misplaced dose, lowering the maximum dose, but dramatically increasing the volume of healthy tissue with assigned dose compared to only respiratory motion. Although normal liver tissue receives high single voxel doses, Tables 3 and 4 shows that in an idealized situation D_{10} is always below 30 Gy, which means that 90 % of the healthy liver tissue receives a dose of less than 30 Gy. The corresponding D_{25} is below 10 Gy, and the 50 % dose fraction was below 1 Gy (data not shown). The dose value (D_{25}) which 75 % of the volume receives a dose less than, is in fact below 10 Gy in all scenarios.

In our simulations, we have assumed a 90/10 % tumor to healthy liver tissue capillaries microsphere distribution, which from the latter results in an average dose to normal tissue of 6 Gy approximately. If the distribution is 60/40 %, the average dose to normal tissue is increased to approximately 25 Gy. These doses will add up with the above mentioned doses.

Discussion

In this study we investigated the effects of respiratory motion during ^{90}Y PET imaging after radio embolization with microspheres. In general, our simulations show that this motion can contribute to under-estimations of tumor doses and over-estimations of normal tissue doses. The largest errors can be expected for smaller tumors. A heterogeneous distribution of microspheres will likely contribute to worse errors for larger tumors.

While PSF blurring effects have been commonly investigated, respiratory motion during ^{90}Y PET imaging has been an area seldom addressed for any dosimetry study. It could seem desirable to establish a framework of "motion coefficients" to correlate a measured value to actual dose values, similar to recovery coefficients commonly used for intensity diffusion (or partial volume effect) correction (7). Given the range of physiological and technical elements influencing the extend of the blurring effects, the intent of the current study was limited to demonstrate the potential errors caused by respiratory motion. Therefore, some simplifications were performed, i.e. blurring the activity distributions directly instead of reconstructing blurred acquisitions. However, it is likely that patient specific variations in breathing pattern or vascularization (affecting tumor microsphere distribution) will probably account for the largest uncertainties in measured-to-actual values.

For our set of parameters, the respiratory motion could have just as large an impact as the geometric resolution for the dose values. To which extend each blurring effect contributes will depend on several factors. For PSF blurring the PET scanner's geometric resolution, the clinical voxel size, TOF versus non-TOF, the spatial PSF distribution will all have an effect. One approach of compensating for this is de-convolution, and our image scenario 2 (respiratory movement only) represents a situation where the geometric blurring is non-existing or accurately corrected. This is interesting because several attempts have been made to compensate for image intensity spreading for dosimetric purposes (4, 9, 10), whilst not regarding patient respiration. While such correction can contribute to more accurate tumor doses, we have demonstrated that it actually can result in the highest max dose and D_{10} values to normal liver tissue, regardless of tumor radius and microsphere distribution. For respiratory blurring, our applied function, simulating movement with a sine function in cranio-caudal direction, is simplistic since the liver

moves in all directions when the patient breathes. In patients, the distant peaks observed for scenario 2 and 3 in Fig. 2 would therefore be more smeared out or completely absent, and the additional blurring would probably contribute to further under-estimation of tumor doses. Adding potential differences in respiration pattern to the uncertainty in microsphere distribution and the scanner & reconstruction specifics further demonstrates the difficulties encountered if introducing correction factors for measured-to-actual dose values.

For molecular radiation therapy the assessment of DVH values (minimum dose to x % of the volume) is of interest to evaluate dose coverage, but it is associated with certain difficulties. We have determined the tumor values using a common "intensity-driven" approach (9), by extracting voxel uptake value from a volume encircling the tumor defined on a PET image. Many of the voxels can then represent normal tissue, but the most intense (as the upper 25 % or 50 %) are likely tumor tissue. However; the mean tumor dose, and perhaps more importantly the D_{90} or D_{98} tumor dose, remains undefined. The other dosimetric approach is to define an anatomical VOI based on CT images, and extract the uptake values from the co-registered PET volume (5, 6). As the CT acquisition is performed in an instant and blurring effects, as illustrated in Fig. 1, will position some ^{90}Y uptake outside this confined area, this approach will also underestimate dose values. (Note that our results for the real dose distribution, scenario 1, in Tables 1 and 2 would be identical regardless of the chosen approach.) Respiratory tracking during both CT and PET, as commonly performed for ^{18}F-FDG PET, seems challenging for ^{90}Y PET due to the low positron abundance.

The rate of Radioembolization Induced Liver Disease for SIRT was reported to be less than 1 % in USA treatment centers (18). Whole liver radiation doses in excess of 30 and 40 Gy delivered by external beam therapy (EBRT) will, in 5 and 50 % of patients respectively, result in liver failure within five years (19, 20). The corresponding dose limit for irradiation of 1/3 of the liver is 50 and 55 Gy. A seemingly discrepancy between EBRT and SIRT complication risks is observed, as SIRT normal tissue doses are commonly found above these limits (6). For our conditions average dose to the liver caused by ^{90}Y microspheres that lodge evenly in non-tumor tissue is 6 Gy. In addition, we estimated D_{10} values of between 5-30 Gy and D_{25} values of < 10 Gy from radiation imparted by nearby tumor tissue (ideal image scenario). The overall normal

tissue dose therefore seems acceptable compared to EBRT (19, 20); however, higher total liver doses can be expected as these doses are imparted from a single tumor (i.e.; 20 % tumor burden and 24 mm radius accounts to 3 tumors in the treated lobe.) Furthermore, non-spherical shaped tumors would impart relatively more radiation on surrounding tissue. The summation of dose charts therefore requires patient-specific information regarding both liver and tumor geometry and reciprocal positioning. Direct comparisons with tolerance limits from EBRT may regardless of a complete liver mapping be difficult to infer due to clustering of microspheres in normal tissue, local dose deposition around each microsphere and radiobiological effects from different dose rates. Nevertheless, the first premise is a correct rendering of the absorbed dose map.

In conclusion, the respiratory movement of the liver during ^{90}Y PET acquisition is perhaps one of the greatest challenges for patient dosimetry, which to our knowledge has not yet been thoroughly discussed. We have in this work demonstrated an underestimation of tumor dose and overestimation of normal liver dose due to mismatch between the imaged and the actual microsphere positions. As the exact values will depend on tumor biology, patient respiratory pattern and scanner specific parameters, no general correction factors between imaged and actual ^{90}Y uptake is suggested.

References

1. Macedo FI, Makarawo T. Colorectal hepatic metastasis: Evolving therapies. World J Hepatol 2014; 6: 453-463.
2. Russell JL, Carden JL, Herron HL. Dosimetry calculations for Yttrium-90 used in the treatment of liver cancer. Endocurie Hypertherm Oncol 1988; 4: 171-186.
3. Sarfaraz M, Kennedy AS, Lodge MA, et al. Radiation absorbed dose distribution in a patient treated with yttrium-90 microspheres for hepatocellular carcinoma. Med Phys 2004; 31: 2449-2453.
4. Lhommel R, van Elmbt L, Goffette P, et al., Feasibility of 90Y TOF PET-based dosimetry in liver metastasis therapy using SIR-Spheres. Eur J Nucl Med Mol Imaging 2010; 37: 1654-1662.
5. Kao YH, Steinberg JD, Tay YS, et al. Post-radioembolization yttrium-90 PET/CT - part 2: dose-response and tumor predictive dosimetry for resin microspheres. EJNMMI Res 2013; 3: 57.
6. Srinivas SM, Natarajan N, Kuroiwa J, et al. Determination of Radiation Absorbed Dose to Primary Liver Tumors and Normal Liver Tissue Using Post-Radioembolization (90)Y PET. Front Oncol 2014; 4: 255.
7. Willowson KP, Tapner M, Team QI, et al. A multicentre comparison of quantitative (90)Y PET/CT for dosimetric purposes after radioembolization with resin microspheres : The QUEST Phantom Study. Eur J Nucl Med Mol Imaging 2015; 42: 1202-1222.
8. Selwyn RG, Nickles RJ, Thomadsen BR, et al. A new internal pair production branching ratio of 90Y: the development of a non-destructive assay for 90Y and 90Sr. Appl Radiat Isot 2007; 65: 318-327.
9. Fourkal E, Veltchev I, Lin M, et al. 3D inpatient dose reconstruction from the PET-CT imaging of 90Y microspheres for metastatic cancer to the liver: feasibility study. Med Phys 2013; 40: 081702.
10. D'Arienzo M, Chiaramida P, Chiacchiararelli L, et al. 90Y PET-based dosimetry after selective internal radiotherapy treatments. Nucl Med Commun 2012; 33: 633-640.
11. Revheim ME, Haugvik SP, Johnsrud K, et al. Respiratory gated and prolonged acquisition 18F-FDG PET improve preoperative assessment of colorectal liver metastases. Acta Radiol 2015; 56: 397-403.
12. Kennedy AS, Nutting C, Coldwell D, et al. Pathologic response and microdosimetry of (90)Y microspheres in man: review of four explanted whole livers. Int J Radiat Oncol Biol Phys 2004; 60: 1552-1563.
13. Campbell AM, Bailey IH, Burton MA. Analysis of the distribution of intra-arterial microspheres in human liver following hepatic yttrium-90 microsphere therapy. Phys Med Biol 2000; 45: 1023-1033.
14. Liu C, Pierce LA 2nd, Alessio AM, et al. The impact of respiratory motion on tumor quantification and delineation in static PET/CT imaging. Phys Med Biol 2009; 54: 7345-7362.
15. Skretting A. A method for on-site measurements of the effective spatial resolution in PET image volumes reconstructed with OSEM and Gaussian post-filters. Radiat Prot Dosimetry 2010; 139: 195-198.
16. Sarfaraz M, Kennedy AS, Cao ZJ, et al. Physical aspects of yttrium-90 microsphere therapy for nonresectable hepatic tumors. Med Phys 2003; 30: 199-203.
17. Berger MJ. Distribution of absorbed dose around point sources of electrons and beta particles in water and other media. J Nucl Med 1971: Suppl 5:5-23.

18. Kennedy AS, McNeillie P, Dezarn WA, et al. Treatment parameters and outcome in 680 treatments of internal radiation with resin 90Y-microspheres for unresectable hepatic tumors. Int J Radiat Oncol Biol Phys 2009; 74: 1494-1500.
19. Emami B, Lyman J, Brown A, et al. Tolerance of normal tissue to therapeutic irradiation. Int J Radiat Oncol Biol Phys 1991; 21: 109-122.
20. Pan CC, Kavanagh BD, Dawson LA, et al. Radiation-associated liver injury. Int J Radiat Oncol Biol Phys 2010; 76: S94-100.

Tables

Table 1: Max dose, and the dose that covers 25% and 50% of the tumor volume for homogeneous microsphere distribution.

Tumor radius (mm)	**6**			**12**			**24**		
Image scenario	**1**	**2**	**3**	**1**	**2**	**3**	**1**	**2**	**3**
MAX (Gy)	217	174	94	232	232	213	232	232	232
D25 (Gy)	173	120	70	223	203	159	232	232	222
D50 (Gy)	135	95	58	193	153	122	227	217	185

Table 2: Max dose, and the dose that covers 25% and 50% of the tumor volume for heterogeneous microsphere distribution.

Tumor radius (mm)	**6**			**12**			**24**			**36**		
Image scenario	**1**	**2**	**3**	**1**	**2**	**3**	**1**	**2**	**3**	**1**	**2**	**3**
MAX (Gy)	598	346	148	383	376	289	414	412	306	516	515	383
D25 (Gy)	215	196	101	342	268	204	362	286	234	414	330	275
D50 (Gy)	102	100	77	179	183	144	201	213	189	167	217	208

Table 3: Max dose, the dose to 10% and 25% of the normal tissue, in addition to volume of healthy liver with positive dose value for homogeneous microsphere distribution.

Tumor radius (mm)	**6**			**12**			**24**		
Image scenario	**1**	**2**	**3**	**1**	**2**	**3**	**1**	**2**	**3**
MAX (Gy)	53	95	64	65	103	94	71	105	102
D10 (Gy)	12	13	0	22	30	1	29	44	7
D25 (Gy)	3	2	0	6	6	0	9	10	0
Vol (ml) liver tissue with positive dose value	11	17	184	29	41	304	88	119	637

Table 4: Max dose, the dose to 10% and 25% of the normal tissue, in addition to volume of healthy liver with positive dose value for heterogeneous microsphere distribution.

Tumor radius (mm)	**6**			**12**			**24**			**36**		
Image scenario	**1**	**2**	**3**	**1**	**2**	**3**	**1**	**2**	**3**	**1**	**2**	**3**
MAX (Gy)	50	199	94	42	139	117	53	157	130	70	198	165
D10 (Gy)	7	9	0	10	14	1	15	26	5	21	39	26
D25 (Gy)	1	1	0	2	2	0	3	5	0	5	8	1
Vol (ml) liver tissue with positive dose value	12	17	188	29	41	310	87	119	640	176	236	776

Figure legends

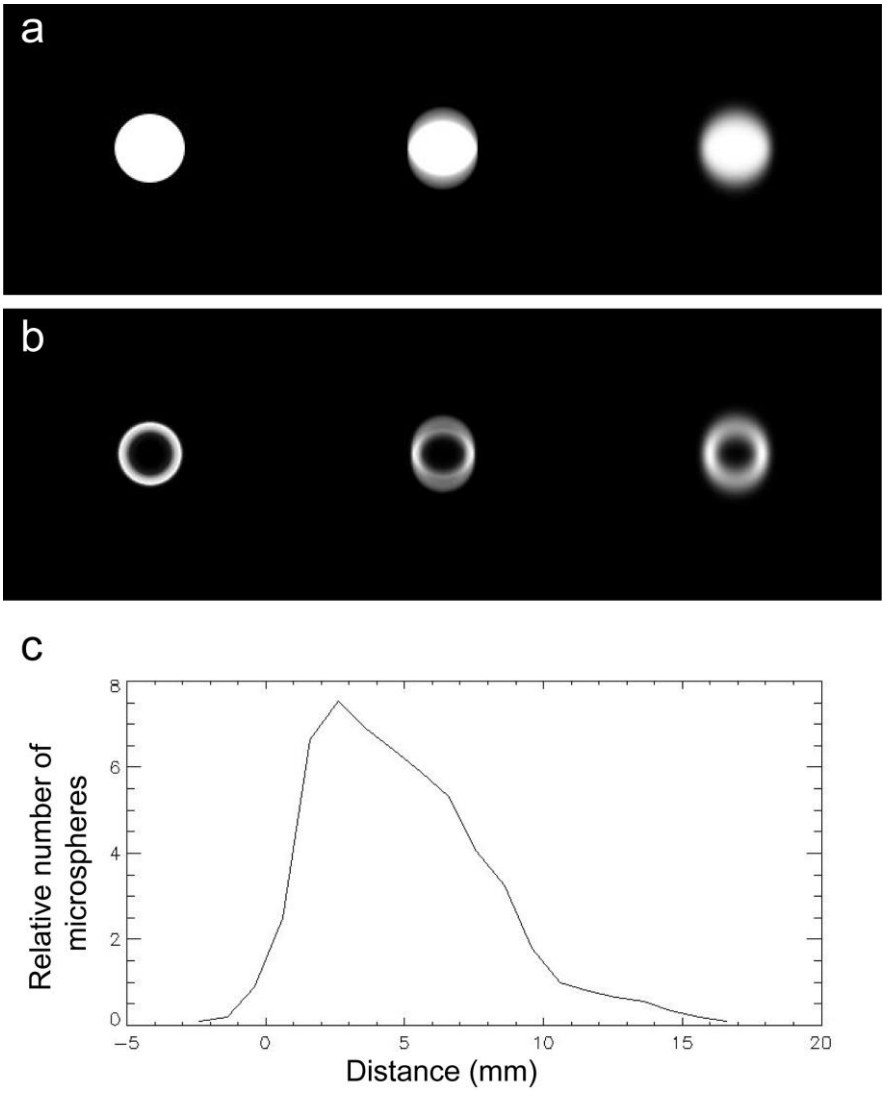

Fig 1. Image simulations of microsphere distribution in spheres of 24 mm radius, homogeneously distributed (a) and heterogeneously distributed (b). Left panel representing image scenario 1 (ideal PET imaging), mid panel image scenario 2 (respiratory movement) and right panel image scenario 3 (respiratory movement plus PSF blurring). (c) The relative microsphere hetrerogeneous distribution as a function of distance from the tumor surface (at 0). The distribution is derived from the study of Campbell et al. (13).

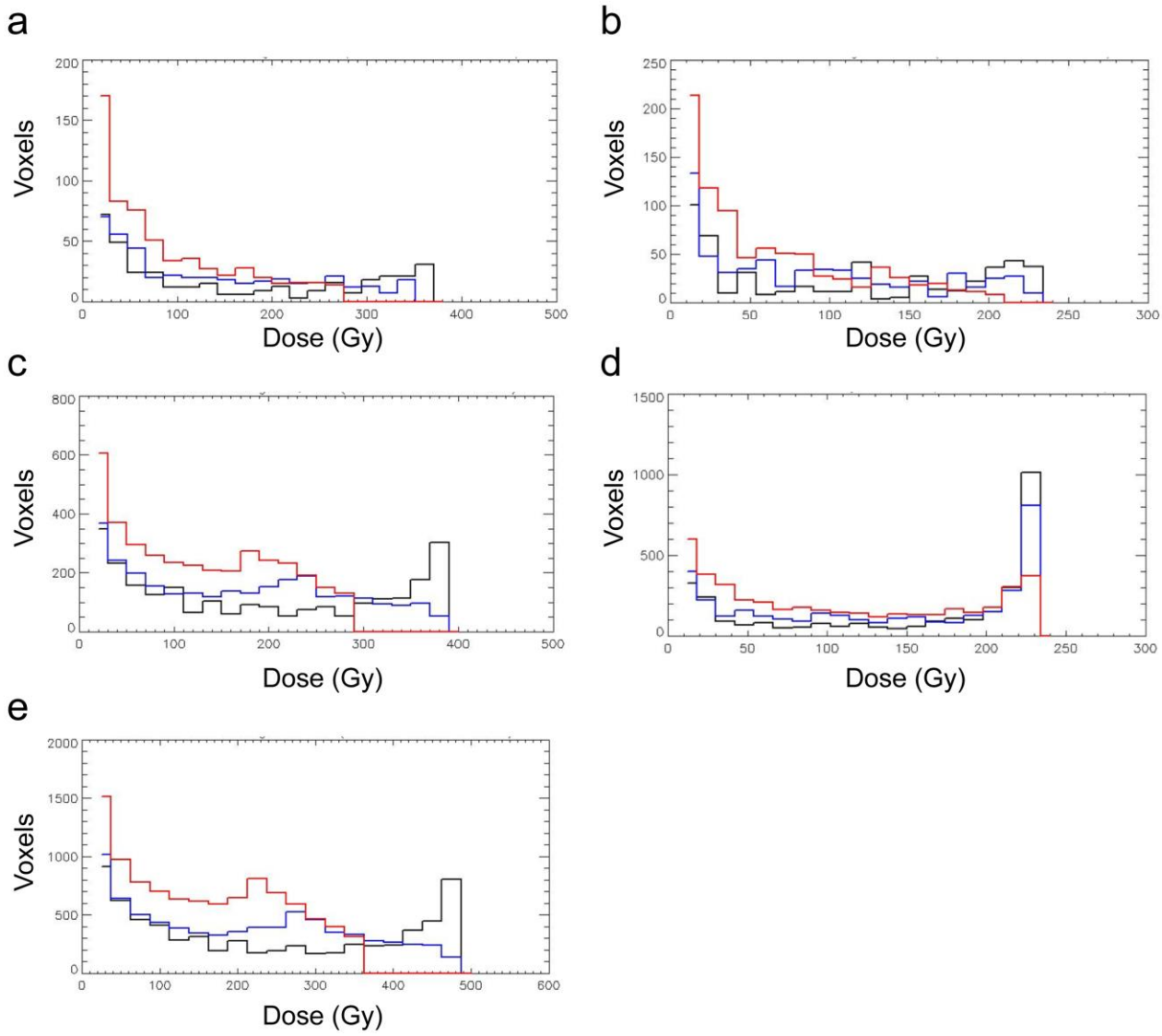

Fig 2. Dose volume histograms for tumors. From the top, the panels represent spheres of 12 mm (a and b), 24 mm (c and d) and 36 mm radius (e), respectively. The left panels (a, c and e) are obtained using heterogeneous microsphere distribution, and the right panels (b and d) homogeneous microsphere distribution. The black plot represents the true dose distribution for the tumor, i.e. ideal PET imaging (scenario 1) , while the blue and red represent the dose distributions obtained when the images are modified by respiratory movement (scenario 2), and respiratory movement plus PSF blurring (scenario 3), respectively.

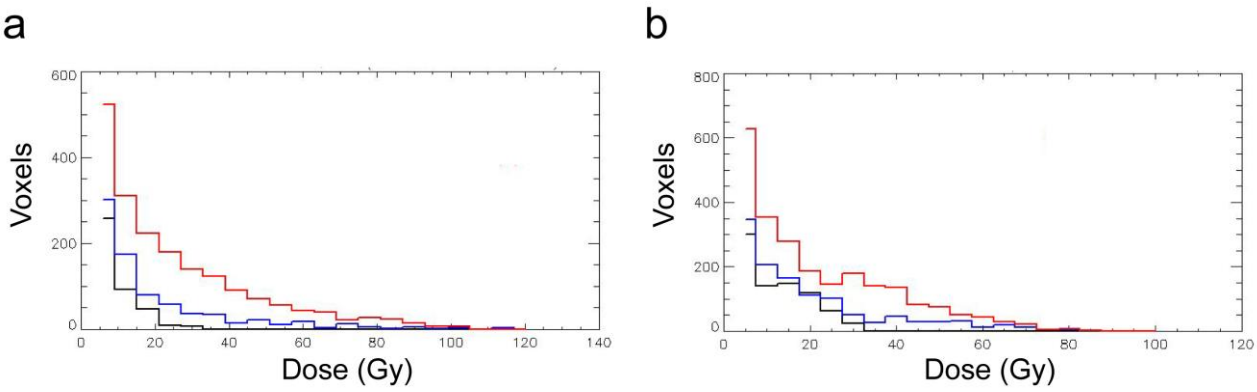

Fig 3. Dose volume histograms for normal liver tissue surrounding a tumor of 24 mm radius. The left panel (a) represents heterogeneously distributed spheres, while the right panel (b) represents the homogeneous distribution. The black, blue and red plot represents the dose distribution around the tumor obtained for scenario 1 (ideal PET imaging), 2 (respiratory movement) and 3 (respiratory movement plus PSF blurring), respectively.